Title

Improved Calcium Scoring at Dual-Energy Computed Tomography Angiography Using a High-Z Contrast Element and Novel Material Separation Technique

Journal

Journal of Computer Assisted Tomography, 42(3)

ISSN

0363-8715

Authors

Lambert, Jack W
Sun, Yuxin
Ordovas, Karen G
et al.

Publication Date

2018-05-01

DOI

10.1097/rct.0000000000000676

Peer reviewed

HHS Public Access

Author manuscript

J Comput Assist Tomogr. Author manuscript; available in PMC 2019 May 01.

Published in final edited form as:

J Comput Assist Tomogr. 2018 ; 42(3): 459–466. doi:10.1097/RCT.0000000000000676.

Improved calcium scoring at Dual-Energy CTA using a high-Z contrast element and novel material separation technique

Jack W. Lambert, PhD, **Yuxin Sun, MSc**, **Karen G. Ordovas, MD**, **Robert G. Gould, ScD**, **Sizhe Wang, MSc**, and **Benjamin M. Yeh, MD**

University of California, San Francisco, 505 Parnassus Ave, San Francisco, CA 94143

Abstract

Objectives—To compare the accuracy of existing Dual-Energy CT angiography coronary artery calcium scoring methods to those obtained using an experimental tungsten-based contrast material and a recently described contrast material extraction process (CMEP).

Methods—Phantom coronary arteries of varied diameters, with different densities and arcs of simulated calcified plaque were sequentially filled with water, iodine and tungsten contrast materials and scanned within a thorax phantom at rapid-kVp-switching Dual-Energy CT. Calcium and contrast density images were obtained by material decomposition (MD) and CMEP. Relative calcium scoring errors among the four reconstructed datasets were compared to a ground truth, 120 kVp dataset.

Results—Compared to the 120 kVp dataset, Tungsten-CMEP showed a significantly lower mean absolute error in calcium score (6.2%, $p<0.001$) than Iodine-CMEP, Tungsten-MD and Iodine-MD (9.9%, 15.7% and 40.8% respectively).

Conclusions—Novel contrast elements and material separation techniques offer improved coronary artery calcium scoring accuracy, and show potential to improve the utility of Dual-Energy CT angiography in a clinical setting.

Keywords

Dual-energy CT; Coronary CT Angiography; calcium; contrast agent; material separation

1. Introduction

Coronary CT Angiography (CCTA) is increasingly used to assess cardiac health, including both the management of stable coronary artery disease (1), and the evaluation of acute coronary syndrome (2). With eight million patients requiring evaluation in the US each year (3), combined with the increased number of indications that can be investigated with CCTA

Corresponding author. Jack W. Lambert, Telephone: 415-514-0507, Fax: 415 476-0616, jack.lambert@ucsf.edu.

Jack W. Lambert. No disclosures to report.

Yuxin Sun. No disclosures to report

Karen G. Ordovas. Salary support from General Electric.

Robert G. Gould. Scientific Advisor, AlgoMedica Inc. Stockholder, General Electric.

Sizhe Wang. No disclosures to report.

Benjamin M. Yeh. Author with Royalties, Oxford University Press. Shareholder, Nextrast Inc.

(4), population radiation exposure is a key concern (2). The radiation concerns for CCTA are heightened by the frequent requirement for two separate exam phases; a non-contrast coronary artery calcium scoring (CACS) phase is often performed prior to the contrast enhanced CTA scan (5–7). Calcium scoring is precluded following the administration of iodinated contrast material at single energy CT (SECT) because iodine and calcium may show indistinguishably high CT numbers (HU) in the reconstructed images (8). Conversely, the degree of arterial stenosis may be misjudged when calcified plaque is present as it is difficult to distinguish calcium from intraluminal iodinated contrast (9). The acquisition of separate CACS and CTA phases results in an increased patient radiation burden and also lengthens the exam time.

Dual-energy CTA (DE-CTA) has emerged as a potential means to reduce radiation dose and improve diagnostic performance for CCTA via generation of virtual non-contrast images which may potentially replace the true non-contrast scans used for calcium scoring (8, 10–14). DE-CTA exploits the difference in the attenuation profile of different elements at low and high X-ray energies in order to discriminate between them and produce virtual non-contrast (8, 13, 14), or calcium-specific (10–12) images that reveal the calcified plaque while suppressing the signal of contrast material. However, the reported results are commonly presented as correlations between SECT and DECT calcium scores (12–14); a somewhat facile metric for CACS which may not reflect the wide agreement limits observed between absolute scores (13–15). Scoring inaccuracies may lead to ambiguity in risk group stratification, patient triage, and disease monitoring.

Recently, several publications have shown the potential benefits of contrast materials using high atomic number (high-Z) elements to provide X-ray attenuation for CT and DECT (16–19). Unlike iodine and calcium, which both show a marked loss of X-ray attenuation at high kVp CT settings, the high-Z elements provide sufficient X-ray attenuation across the range of kVp settings used for DECT. The signal of high-Z contrast agents can thus be readily separated from the signal of calcium (18–20). While the utility of high-Z contrast agents has been shown in preclinical animal models of abdominal disease (21, 22), their performance for quantitative separation tasks such as CACS remain unknown. Also, novel algorithms to separate contrast material signal from calcium at DECT have been described (23, 24), and include the contrast material extraction process (CMEP) (25). CMEP, an image domain material separation method that offers an alternative to conventional material decomposition (MD), showed accurate separation of contrast agent signals in a phantom study (25), but has not been tested for CACS. We hypothesize that the use of a high-Z contrast material and CMEP could offer improved CACS accuracy compared to conventional iodine contrast material and MD image processing.

Therefore, the purpose of our pilot study was to compare relative accuracies of existing CACS at DE-CTA to those derived using a high-Z contrast element or CMEP. Our hypothesis was that more accurate calcium scores could be achieved using these novel methods.

2. Methods

2.1 Phantom

A thorax phantom was constructed specifically to test DE-CTA (Fig 1). The phantom measured 300 × 200 × 100 mm in the x- y- and z-dimensions and was composed of urethane rubber, which has a CT number of −5 HU, similar to that of water, at 120 kVp. Polystyrene foam inserts were used to simulate the lungs, and a calcium-doped urethane rubber insert was used to simulate the spine. A central 110 mm diameter mediastinal insert containing seven sets of 3, 6, and 9 mm diameter cylindrical holes in a radial pattern simulated a range of typical coronary artery lumen sizes. Annular calcified “plaque”, 1.5 mm thick, was simulated using calcium hydroxyapatite (HAP)-doped urethane rubber. The urethane rubber used for the calcifications contained 5% magnesium to provide an energy-independent CT number of ~5 HU at DECT (*i.e.* a neutral base material with properties similar to water at 80 to 140 kVp). Three of the seven inserts modeled concentric calcifications at concentrations of 20, 40, and 60% HAP by weight (Fig 1, A 1–3), while three modeled eccentric calcifications with an arc of 120° and the same HAP densities (Fig 1 A, 4–6). These concentrations corresponded to CT numbers of ~250, ~400 and ~550 HU at 120 kV single energy. The final vessel set was an uncalcified control set (Fig 1 A, 7).

2.2 CT scanning

The phantom was imaged using a rapid-kVp-switching DECT scanner (Discovery CT750 HD; GE Healthcare, Waukesha, WI) in helical mode with a collimation of 40 mm (64 × 0.625 mm detector rows), a pitch of 1.375:1, a rotation time of 0.5 s, a large body filter, and a tube current of 360 mA, resulting in a CTDIvol of 7.3 mGy. The phantom was filled sequentially with a clinical iodinated contrast material iohxeol ($C_{19}H_{26}I_3N_3O_9$) (Omnipaque 350; GE Healthcare), and a non-clinical sodium tungsten dihydrate ($Na_2WO_4 \cdot {}_2H_2O$) contrast material. This tungsten compound is not viable for development due to toxicity, but is inexpensive, water soluble, and has the same X-ray attenuation characteristics as potentially viable tungsten-based agents. The contrast materials were formulated in distilled water to concentrations of 10 mg/mL of the active element (20, 26, 27) which provided a contrast enhancement of ~280 HU for both elements at 120 kVp. Although higher contrast enhancement in the coronary arteries can be achieved clinically (28), we chose a relatively low concentration of 10 mg/mL for two reasons. First, we wanted to provide a challenging problem for material separation, as this task becomes more straightforward with increasing elemental concentration (29). Second, since DE-CTA enables superior contrast resolution (30, 31), administration of lower contrast agent doses and correspondingly lower CT numbers is likely in the future, compared to those currently observed with conventional single energy CTA. SECT at 120 kVp was also performed with water in the vessel lumens, with the tube current set to match the 7.3 mGy CTDIvol of the dual-energy acquisitions. All images were reconstructed with a 25 cm field-of-view at a contiguous thickness of 2.5 mm, as used clinically.

2.3 Image processing

2.3.1 Material Decomposition—The calcium and contrast materials were decomposed into material pair datasets with a thickness of 2.5 mm using commercial two-MD software

(GSI Viewer, Advantage Windows Workstation 4.4; GE Healthcare). For the iodine contrast, an MD pair was defined using iohexol rather than the default iodine material to improve fidelity (10, 11), and correspondingly using HAP rather than elemental calcium for the other material. For the tungsten contrast, an empirically determined pseudo-tungsten material was implemented for the MD. Such an approach is required as this software is currently unable to decompose elements with a k-edge between 40 and 140 keV (tungsten k-edge = 69.5 keV) (21, 22). Pseudo-tungsten was defined with a linear slope of decreasing attenuation coefficient from 1 to 0 cm^2/g over the 40 to 140 keV energy range. Although this linear slope has no physical basis, it was determined through trial and error to provide the best separation of the calcifications from the tungsten contrast. An important consideration for two-MD is that any defined material is linked to the material it is paired with, in this instance HAP, as only those two materials are considered to be present in the volume. This pseudo-tungsten slope therefore represents an ad-hoc solution for this specific material pair, and as such its use should not be extrapolated to any other decomposition tasks. MD images required scaling from their default output in mg/cm^3 concentrations to CT numbers, to enable conventional CACS. This was achieved via linear regression (8), using the background urethane rubber CT number and maximum calcium CT number as the two scaling points.

2.3.2 Contrast Material Extraction Process—The Contrast Material Extraction Process (CMEP) selectively extracts contrast producing materials in the dataset based on their dual energy ratio; the ratio of CT numbers from low to high x-ray energies (25). Thresholded masks are created from the dual energy ratio map, and are subsequently applied to original CT images to generate material specific images. Accordingly, the input parameters for the process are the dual energy ratio ranges corresponding to the desired separation materials, and image datasets at three different x-ray energies. Low and high-energy datasets are required to generate the ratio map, while a synthesized medium energy dataset is used for creation of the final material-specific images from the masks. Aside from initial generation of the image datasets using vendor software, CMEP is performed within the Fiji freeware (NIH, Bethesda, MD) (32). In our study the ratio ranges were defined as 0.5 – 1.2, for tungsten, 1.4 – 1.6 for calcium, and 1.8 – ∞ for iodine. These ratio ranges were approximated from different literature sources (25, 33, 34) and validated empirically for the phantom set-up used. For the three image datasets, 60 keV, 80 keV and 67 keV were used for the E1, E2 and E3 inputs respectively. As in previous work, the 60 and 80 keV levels were chosen as they approximate the mean photon energies of the physical 80 and 140 kVp spectra (33, 34). A 67 keV virtual monochromatic spectral level was chosen for E3 as it is has been shown to match the 120 kVp CT numbers of bone (35).

2.4 Image analysis

Material-specific images were assessed qualitatively for the overall fidelity of the contrast and calcium maps. For quantitative scoring of the calcium images, the four DECT material-specific datasets; Iodine-MD, Iodine-CMEP, Tungsten-MD and Tungsten-CMEP were compared against ground truth SECT at 120 kVp, with water in the simulated vessels (Fig 1 A). Circular regions of interest (ROIs) were placed over each of the calcifications in eight consecutive images for a total of 144 calcification measurements in each dataset (3

calcification sizes × 3 calcification densities × 2 calcification types × 8 images). For each ROI a calcium score, calcium volume and calcium mass was calculated. For the calcium score, the standard Agatston technique was used, where the maximum CT number within each calcification is multiplied by its area generate a score (36). For the calcium volume score, the calcification area (pixels with a CT number above the threshold of 130 HU) was measured and multiplied by the 2.5 mm pixel thickness to provide a volume (37). No volume interpolation methods were used, as the calcifications were nominally constant through the thickness of the phantom (38). For the calcium mass score, the calcium volume for each calcification was multiplied by its mean CT number (37). Calcium mass scores were divided by 100 to bring them in line with the other scores (39). We present all three scores as unitless integer score values (39), rather than attempting to convert to volumes or concentrations (15). Results were then grouped by calcification size, calcification type, contrast element and separation method to assess trends among each. Statistical significance was assessed using Bonferroni-corrected matched paired t-tests and Welch's t-tests. Matched paired t-tests were used to assess the differences between the four material-specific datasets and the ground truth 120 kVp dataset. Welch's t-tests, which do not assume equal variance, were used to assess differences among the percentage errors of the data when grouped by calcification density, size and type. Differences were considered to be significant if $p<0.05$ in a two-tailed distribution.

3. Results

3.1 Qualitative Analysis

The material separation was qualitatively successful for both iodine and tungsten, and for both MD and CMEP (Fig 2). Some false positive iodine signal was visible in the calcified vessel walls for the iodine MD image (Fig 2 A) as well as in the air, as observed previously (22). This false positive contrast signal was absent for the tungsten MD image, which had a well-defined lumen-wall interface (Fig 2 E). The corresponding calcium MD images both showed the calcifications clearly, with no false positive signal in the lumens (Fig 2 B,F). While the calcium-iodine MD image (Fig 2 B) appeared slightly sharper, the low-density calcifications were more readily depicted in the calcium-tungsten MD image (Fig 2 F). The CMEP images showed the black "zero" value backgrounds typical of the process, as only positive (> 0 HU) contrast is extracted (25). It should be noted, however, that other image types (*e.g.* a virtual non-contrast water image) could easily be added to the dataset as an overlay if anatomical reference is needed. Iodine and tungsten CMEP images performed comparably (Fig 2 C,G). In the calcium CMEP images, calcium-tungsten (Fig 2 H) outperformed calcium-iodine (Fig 2 D). CMEP calcium-iodine (Fig 2 D) shows an underestimation of calcium, as well as a slight false positive signal in the uncalcified control set, although the majority of this signal is below the 130 HU threshold for scoring.

3.2 Quantitative Analysis

3.2.1 Calcium scores—Calcium scores, which are based on the area and maximum CT number of the calcifications, ranged from 31, for the 3 mm, 20% HAP, eccentric calcification to 342 to for the 9 mm, 60% HAP, concentric calcification (Table 1). Grouping the data from Table 1, mean absolute errors for the four datasets were 39.8%, 9.7%, 16.3%

and 6.4% for the Iodine-MD, Iodine-CMEP, Tungsten-MD and Tungsten-CMEP respectively ($p<0.001$ between all datasets) (Fig 3). Grouping by calcification density showed increasing scoring accuracy with increasing calcium density, with mean absolute errors of 31%, 14% and 10% for the 20%, 40% and 60% HAP calcifications ($p<0.001$ between 20% and 60% HAP). Grouping by size gave consistent results, with mean absolute errors of 19%, 19% and 17% for the 3 mm, 6 mm and 9 mm calcifications respectively ($p>0.2$). Grouping by calcification type also gave consistent results, with a mean absolute error of 18% for both concentric and eccentric calcifications ($p>0.2$).

3.2.2 Calcification volume scores—Calcium volume scores, which are based on the area of the calcifications, ranged from 26 for the 3 mm, 20% HAP, eccentric calcification to 214 to for the 9 mm, 60% HAP, concentric calcification (Table 2). Grouping the data from Table 2, the mean absolute errors for the four datasets were 35.2%, 9.5%, 16.4% and 6% for the Iodine-MD, Iodine-CMEP, Tungsten-MD and Tungsten-CMEP respectively ($p<0.001$ between all datasets) (Fig 3). Grouping by calcification density showed the same trend as the calcium scores, with mean absolute errors of 27%, 13% and 10% for the 20%, 40% and 60% HAP calcifications respectively ($p<0.001$ between 20% and 60% HAP). Grouping by size showed consistent mean absolute errors of 17%, 18% and 16% for the 3 mm, 6 mm and 9 mm calcifications respectively ($p>0.2$). Grouping by calcification type also provided a consistent mean error of 17% for both concentric and eccentric calcifications ($p>0.2$).

3.2.3 Calcium mass scores—Calcium mass scores, which are based on the product of the area and mean CT number of the calcifications, ranged from 59 for the 3 mm, 20% HAP, eccentric calcification to 980 to for the 9 mm, 60% HAP, concentric calcification (Table 3). Grouping the data from Table 3, the mean absolute errors for the four datasets were 47.3%, 10.4%, 14.5% and 6.2% for the Iodine-MD, Iodine-CMEP, Tungsten-MD and Tungsten-CMEP respectively ($p<0.001$ between all datasets) (Fig 3). Grouping by calcification density showed the same trend as the others scores, with mean absolute errors of 30%, 17% and 11% for the 20%, 40% and 60% HAP calcifications ($p<0.05$ between all datasets). Grouping by size showed consistent mean absolute errors of 19%, 20% and 19% for the 3 mm, 6 mm and 9 mm calcifications respectively ($p>0.2$). Grouping by calcification type again provided consistent absolute mean errors of 20% for concentric and 19% eccentric calcifications ($p>0.2$).

3.2.4 Grouped score data—Grouping the data from the different calcium scoring methods (Fig 3) by contrast element, the mean absolute errors were 25.3% and 10.9% for iodine and tungsten respectively ($p<0.001$). Grouping the data from the different calcium scoring methods by material separation dataset, the mean absolute errors were 40.8%, 9.9%, 15.7% and 6.2% for Iodine-MD, Iodine-CMEP, Tungsten-MD and Tungsten-CMEP respectively ($p<0.001$ between all datasets). Further grouping this data by material separation method, the mean absolute errors were 28.2% and 8% for MD and CMEP respectively ($p<0.001$).

4. Discussion

We developed a semi-anthropomorphic thorax phantom with simulated calcified “plaque”, and used it to test for relative CACS accuracy at DE-CTA. The phantom was imaged with conventional iodinated contrast material versus a novel, high atomic number contrast element, and the images were analyzed using commercial material decomposition software versus a novel material separation method. The novel contrast element, tungsten, and the novel material separation method, CMEP, both improved accuracy over the conventional techniques, when compared to a ground truth 120 kVp single energy dataset. This result was consistent across the different calcium scoring types evaluated, with the same ranked order of decreasing accuracy from Tungsten-CMEP, through Iodine-CMEP, Tungsten-MD to Iodine-MD for the three scores. Quantitative accuracy was confirmed through comparison of absolute values, rather than the less rigorous correlation analyses which have been used previously (12–14).

The first major finding of our work was the improved calcium separation from tungsten compared to from iodine, for both MD and CMEP. We believe that this is due to iodine and calcium behaving more similarly to one another at DECT compared to tungsten and calcium, which are more readily separated. This is suggested by their respective dual energy ratios; tungsten has a dual energy ratio of ~1, calcium a ratio of ~1.5 and iodine a ratio of ~2 (18, 20, 33). Although the absolute difference between each is 0.5, the percentage difference is 50% for tungsten-calcium and only 33% for iodine-calcium. This greater relative difference in dual energy ratio enables the improved separation performance of tungsten, and can be evidenced directly for CMEP, where dual energy ratios are used as the primary input for the process (25). The link is less obvious for MD, where proprietary algorithms are used to produce the material pairs.

Although the sodium tungstate solution used in our study is not viable for clinical translation, a study using D-glucuronic acid-coated sodium tungstate nanoparticles has shown superior attenuation properties and biocompatibility (40). In addition, development of tungsten trioxide (WO_3) nanoparticle agents, coated with either chitosan (41) or poly-ε-caprolactone (42) display similar properties that are promising for further development. Agents based on several other high-Z elements such as gold (43) ytterbium (44), bismuth (45), tantalum (46) and hafnium (47) have also been proposed. Such agents would share the properties exhibited by tungsten, as most high-Z elements also show dual energy ratios of ~1 (18, 34). Gadolinium, a common contrast element used for MRI scanning, would not share these properties as its dual energy ratio of ~1.4–1.7 (33, 34) is within the same range as calcium, and as such the two elements are inseparable at DECT. Gadolinium also raises toxicity and retention concerns, particularly for the large injected doses required for use as a CT contrast agent compared to MRI (19, 48). Further benefits offered by high-Z contrast elements include greater attenuation and thus brighter image contrast (16, 17, 49), good tolerability (46, 47), utility in double contrast DECT studies (18, 21, 22, 50), and compatibility with metal artifact reduction (27). Agents based on these elements are still however in preclinical toxicity testing stages, with a hafnium chelate (47) and a tantalum nanoparticle-based agent (46) appearing most promising for clinical translation in the medium term. Preclinical injected elemental concentrations of 300 mg/mL and 140 mg/mL

have been achieved for hafnium and tantalum respectively, with favorable toxicity results compared to iodine (46, 47). Both agents remain several years from clinical introduction, however, as safety requirements for intravenously injected contrast agents remain demanding, and regulatory hurdles stringent (19).

The second major finding of our work was the improved accuracy of CMEP compared to MD. Using MD, all the pixel brightness is forced to belong to one material or another, and as such small variations in default, or user-defined material attenuation profiles can result in large under or over-estimation of each material (22, 25). At DE-CTA, a systematic underestimation of calcium is prevalent (12–15), and was again observed in our study. This underestimation of calcium occurs regardless of which MD image type is chosen; water-iodine, calcium-iodine or “material suppressed iodine” (12). In our current study, calcium underestimation persisted despite the use of more a representative material pair; iohexol-HAP, rather than elemental iodine and calcium. In addition to improved CACS accuracy, a further advantage of CMEP is that scaling of the output is not needed; 67 keV was chosen as the energy level for the CMEP material-specific images as it had been shown previously to most closely match 120 kVp images for calcium (35). As a result, the CT numbers were in close agreement without the calibration factors that are required for MD images (8, 11–13, 51).

The third major finding of our work was the successful development of a thorax phantom for the screening of different contrast agents, specifically their performance at DE-CTA. When filled with water, the phantom can also be used for the calibration of calcium quantities, with its known HAP densities and volumes (10, 51). The 18 distinct vessel lumen sizes, calcification densities and types represent a wide range of clinically relevant simulated plaques. Importantly, there is a direct interface between the calcifications and the contrast agent (52), providing a more challenging and clinically relevant material separation task than could be achieved using a simpler phantom with separate material vials.

The theoretical dose saving from the use of DECT in our study was 50%, as we matched the CTDIvol for the non-contrast single energy scan to that of the DE-CTA scan. As such the elimination of the non-contrast calcium scoring phase would halve the radiation dose. In practice, lower doses can be used for the calcium scoring compared to the CTA phase, and clinical dose reductions from the adoption of DE-CTA for calcium scoring have ranged from 7% (14), through 20% (13), 33% (15) to 37% (53). This wide range is due to differences in inter-institution CT protocols, including parameters such as bolus tracking, ECG gating and scan length. However though dose savings may be more modest than 50%, further benefits offered by DECT in cardiac applications have been noted as lower image noise (13), reduced beam hardening (54), improved image quality in patients with coronary stents (55) and specific plaque component characterization (53).

Our study had several limitations. First, it was a static (non-pulsatile) phantom study, and as such the wide variety, patterns and motion of calcium burdens that are observed clinically could not be evaluated. In addition, the influence of patient-specific scan parameters such as cardiac gating and bolus timing could not be ascertained. This was unavoidable as no high-Z contrast agents have been approved for clinical use (18, 19, 56). CMEP has however been

shown to work *in vivo* using a rabbit model, with the separation of iodine, tungsten and calcium (25). A benefit of using a phantom was the direct comparison that was achieved with ground truth 120 kVp data, without the additional patient radiation dose and variable motion artifact confounders that would occur with human scanning (13). Second, only rapid-kVp-switching DECT was assessed, and results may not directly translate to dual source or dual layer DECT. Nevertheless, similar CMEP and MD results have been reported for both rapid-switching and dual source CT (25). One uncertainty is the 67 keV level that was chosen as the basis for the CMEP output, which is likely to be specific to this scanner model. Third, only a single material type, HAP, was used to simulate the calcifications. Our study therefore lacks an appreciation for the other components of coronary calcifications, such as calcium oxalate monohydrate (53) and also non-calcified coronary plaques (10). Fourth, for practical reasons, a single representative high-Z element (tungsten) was tested rather than a range of high-Z elements. Prior studies of high-Z elements at CT and DECT also used a representative element approach since the X-ray attenuation properties of high-Z elements with similar atomic number resemble one another (16, 18, 20).

In conclusion, high-Z contrast elements currently in development may offer improved calcium scoring accuracy at dual-energy CTA compared to conventional iodinated agents as a result of their distinct attenuation profiles. In addition, a recently defined, image-based material separation technique also has the ability to enhance calcium scoring accuracy through direct use of dual energy ratios, when applied to both conventional or novel contrast agents. The improvements made available by each may significantly reduce the current error margins observed clinically.

Acknowledgments

Research reported in this manuscript was supported by the National Institutes of Health under the award numbers R01EB015476, 1R41DK104580 and UCSF-CTSI UL1 TR000004. The content is solely the responsibility of the authors and does not necessarily represent the official views of the National Institutes of Health.

References

1. Montalescot G, Sechtem U, Achenbach S, et al. 2013 ESC guidelines on the management of stable coronary artery disease. Eur Heart J. 2013; 34(38):2949–3003. [PubMed: 23996286]
2. Staniak HL, Bittencourt MS, Pickett C, et al. Coronary CT angiography for acute chest pain in the emergency department. J Cardiovasc Comput Tomogr. 2014; 8(5):359–67. [PubMed: 25301041]
3. Goldstein JA, Chinnaiyan KM, Abidov A, et al. The CT-STAT (Coronary Computed Tomographic Angiography for Systematic Triage of Acute Chest Pain Patients to Treatment) trial. J Am Coll Cardiol. 2011; 58(14):1414–22. [PubMed: 21939822]
4. den Harder AM, Willemink MJ, de Ruiter QM, et al. Dose reduction with iterative reconstruction for coronary computed tomography angiography: a systematic review and meta-analysis. Br J Radiol. 2015:20150068. [PubMed: 26562096]
5. Leschka S, Scheffel H, Desbiolles L, et al. Combining dual-source computed tomography coronary angiography and calcium scoring: added value for the assessment of coronary artery disease. Heart. 2008; 94(9):1154–61. [PubMed: 18032458]
6. van Werkhoven JM, Schuijf JD, Gaemperli O, et al. Incremental prognostic value of multi-slice computed tomography coronary angiography over coronary artery calcium scoring in patients with suspected coronary artery disease. Eur Heart J. 2009; 30(21):2622–9. [PubMed: 19567382]
7. Versteylen MO, Joosen IA, Winkens MH, et al. Combined use of exercise electrocardiography, coronary calcium score and cardiac CT angiography for the prediction of major cardiovascular

events in patients presenting with stable chest pain. Int J Cardiol. 2013; 167(1):121–5. [PubMed: 22225760]

8. Fuchs TA, Stehli J, Dougoud S, et al. Coronary artery calcium quantification from contrast enhanced CT using gemstone spectral imaging and material decomposition. Int J Cardiovasc Imaging. 2014; 30(7):1399–405. [PubMed: 24993390]
9. Zhang S, Levin DC, Halpern EJ, et al. Accuracy of MDCT in assessing the degree of stenosis caused by calcified coronary artery plaques. American Journal of Roentgenology. 2008; 191(6): 1676–83. [PubMed: 19020235]
10. Pavlicek W, Panse P, Hara A, et al. Initial use of fast switched dual energy CT for coronary artery disease Proc of SPIE Vol. 7622 76221V-2, 2010. International Society for Optics and Photonics: 76221V-1.
11. Yamak D, Pavlicek W, Boltz T, et al. Coronary calcium quantification using contrast-enhanced dual-energy computed tomography scans. J Appl Clin Med Phys. 2013; 14(3)
12. Song I, Yi JG, Park JH, et al. Virtual Non-Contrast CT Using Dual-Energy Spectral CT: Feasibility of Coronary Artery Calcium Scoring. Korean journal of radiology. 2016; 17(3):321–9. [PubMed: 27134521]
13. Yamada Y, Jinzaki M, Okamura T, et al. Feasibility of coronary artery calcium scoring on virtual unenhanced images derived from single-source fast kVp-switching dual-energy coronary CT angiography. J Cardiovasc Comput Tomogr. 2014; 8(5):391–400. [PubMed: 25301045]
14. Schwarz F, Nance JW Jr, Ruzsics B, et al. Quantification of coronary artery calcium on the basis of dual-energy coronary CT angiography. Radiology. 2012; 264(3):700–7. [PubMed: 22829684]
15. Fuchs TA, Stehli J, Dougoud S, et al. Coronary artery calcium quantification from contrast enhanced CT using gemstone spectral imaging and material decomposition. Int J Cardiovasc Imaging. 2014; 30(7):1399–405. [PubMed: 24993390]
16. FitzGerald PF, Colborn RE, Edic PM, et al. CT Image Contrast of High-Z Elements: Phantom Imaging Studies and Clinical Implications. Radiology. 2016; 278(3):723–33. [PubMed: 26356064]
17. Roessler AC, Hupfer M, Kolditz D, et al. High Atomic Number Contrast Media Offer Potential for Radiation Dose Reduction in Contrast-Enhanced Computed Tomography. Invest Radiol. 2016; 51(4):249–54. [PubMed: 26606552]
18. Falt T, Soderberg M, Wasselius J, Leander P. Material Decomposition in Dual-Energy Computed Tomography Separates High-Z Elements From Iodine, Identifying Potential Contrast Media Tailored for Dual Contrast Medium Examinations. J Comput Assist Tomogr. 2015; 39(6):975–80. [PubMed: 26295191]
19. Yeh BM, FitzGerald PF, Edic PM, et al. Opportunities for new CT contrast agents to maximize the diagnostic potential of emerging spectral CT technologies. Adv Drug Deliv Rev. 2016 In Press.
20. Lambert JW, FitzGerald PF, Edic PM, et al. The Effect of Patient Diameter on the Dual-Energy Ratio of Selected Contrast-Producing Elements. J Comput Assist Tomogr. 2016
21. Mongan J, Rathnayake S, Fu Y, et al. In vivo differentiation of complementary contrast media at dual-energy CT. Radiology. 2012; 265(1):267–72. [PubMed: 22778447]
22. Rathnayake S, Mongan J, Torres AS, et al. In vivo comparison of tantalum, tungsten, and bismuth enteric contrast agents to complement intravenous iodine for double-contrast dual-energy CT of the bowel. Contrast media & molecular imaging. 2016
23. Mendonca PR, Lamb P, Sahani DV. A Flexible Method for Multi-Material Decomposition of Dual-Energy CT Images. IEEE Trans Med Imaging. 2014; 33(1):99–116. [PubMed: 24058018]
24. Long Y, Fessler JA. Multi-material decomposition using statistical image reconstruction for spectral CT. IEEE Trans Med Imaging. 2014; 33(8):1614–26. [PubMed: 24801550]
25. Lambert JW, Sun Y, Gould RG, et al. An Image-Domain Contrast Material Extraction Method for Dual-Energy Computed Tomography. Invest Radiol. 2017; 52(4):245–54. [PubMed: 27875338]
26. FitzGerald PF, Colborn RE, Edic PM, et al. CT Image Contrast of High-Z Elements: Phantom imaging studies and clinical implications. Radiology. 2016; 278(3):723–33. [PubMed: 26356064]
27. Lambert JW, Edic P, Fitzgerald PF, et al. Complementary contrast media for metal artifact reduction in Dual-Energy CT. J Med Imaging. 2015; 2(3):033503.

28. Masuda T, Funama Y, Imada N, et al. Prediction of Aortic Enhancement on Coronary CTA Images Using a Test Bolus of Diluted Contrast Material. Acad Radiol. 2014; 21(12):1542–6. [PubMed: 25442352]
29. Tran DN, Straka M, Roos JE, et al. Dual-energy CT discrimination of iodine and calcium: experimental results and implications for lower extremity CT angiography. Acad Radiol. 2009; 16(2):160–71. [PubMed: 19124101]
30. Machida H, Tanaka I, Fukui R, et al. Current and novel imaging techniques in coronary CT. Radiographics. 2015; 35(4):991–1010. [PubMed: 26046942]
31. Fuchs TA, Stehli J, Fiechter M, et al. First experience with monochromatic coronary computed tomography angiography from a 64-slice CT scanner with Gemstone Spectral Imaging (GSI). J Cardiovasc Comput Tomogr. 2013; 7(1):25–31. [PubMed: 23452997]
32. Schindelin J, Arganda-Carreras I, Frise E, et al. Fiji: an open-source platform for biological-image analysis. Nature methods. 2012; 9(7):676–82. [PubMed: 22743772]
33. Gabbai M, Leichter I, Mahgerefteh S, Sosna J. Spectral material characterization with dual-energy CT: comparison of commercial and investigative technologies in phantoms. Acta Radiol. 2015; 56(8):960–9. [PubMed: 25182803]
34. Lambert JW, FitzGerald PF, Edic PM, et al. The Effect of Patient Diameter on the Dual-Energy Ratio of Selected Contrast-Producing Elements. J Comput Assist Tomogr. 2016
35. Sun, Y., Lambert, JW., Wang, ZJ., et al. Which Dual Energy CT Virtual Monochromatic keV Reconstruction is best to Simulate Typical kVp Settings at Standard CT?. Radiological Society of North America Annual Meeting, SSC05-03; 2016; Chicago, Ill.
36. Agatston AS, Janowitz WR, Hildner FJ, et al. Quantification of coronary artery calcium using ultrafast computed tomography. J Am Coll Cardiol. 1990; 15(4):827–32. [PubMed: 2407762]
37. Ghadri JR, Goetti R, Fiechter M, et al. Inter-scan variability of coronary artery calcium scoring assessed on 64-multidetector computed tomography vs. dual-source computed tomography: a head-to-head comparison. Eur Heart J. 2011; 32(15):1865–74. [PubMed: 21546450]
38. Callister TQ, Cooil B, Raya SP, et al. Coronary artery disease: improved reproducibility of calcium scoring with an electron-beam CT volumetric method. Radiology. 1998; 208(3):807–14. [PubMed: 9722864]
39. Yoon HC, Greaser LE 3rd, Mather R, et al. Coronary artery calcium: alternate methods for accurate and reproducible quantitation. Acad Radiol. 1997; 4(10):666–73. [PubMed: 9344288]
40. Kim SJ, Xu W, Ahmad MW, et al. Synthesis of nanoparticle CT contrast agents: in vitro and in vivo studies. Science and Technology of Advanced Materials. 2015; 16(5):055003. [PubMed: 27877838]
41. Firouzi M, Poursalehi R, Delavari H, et al. Chitosan coated tungsten trioxide nanoparticles as a contrast agent for X-ray computed tomography. Int J Biol Macromol. 2017; 98:479–85. [PubMed: 28174086]
42. Jakhmola A, Anton N, Anton H, et al. Poly-ε-caprolactone tungsten oxide nanoparticles as a contrast agent for X-ray computed tomography. Biomaterials. 2014; 35(9):2981–6. [PubMed: 24393266]
43. Hainfeld J, Slatkin D, Focella T, Smilowitz H. Gold nanoparticles: a new X-ray contrast agent. Br J Radiol. 2006; 79(939):248–53. [PubMed: 16498039]
44. Liu Y, Ai K, Liu J, et al. A high-performance ytterbium-based nanoparticulate contrast agent for in vivo X-ray computed tomography imaging. Angew Chem Int Ed Engl. 2012; 51(6):1437–42. [PubMed: 22223303]
45. Rabin O, Perez JM, Grimm J, et al. An X-ray computed tomography imaging agent based on long-circulating bismuth sulphide nanoparticles. Nature materials. 2006; 5(2):118–22. [PubMed: 16444262]
46. FitzGerald PF, Butts MD, Roberts JC, et al. A Proposed Computed Tomography Contrast Agent Using Carboxybetaine Zwitterionic Tantalum Oxide Nanoparticles: Imaging, Biological, and Physicochemical Performance. Invest Radiol. 2016
47. Frenzel T, Bauser M, Berger M, et al. Characterization of a Novel Hafnium-Based X-ray Contrast Agent. Invest Radiol. 2016; 51(12):776–85. [PubMed: 27299578]

48. Stojanov D, Aracki-Trenkic A, Benedeto-Stojanov D. Gadolinium deposition within the dentate nucleus and globus pallidus after repeated administrations of gadolinium-based contrast agents-current status. Neuroradiology. 2016; 58(5)

49. Nowak T, Hupfer M, Brauweiler R, et al. Potential of high-Z contrast agents in clinical contrast-enhanced computed tomography. Med Phys. 2011; 38(12):6469–82. [PubMed: 22149830]

50. Mongan J, Rathnayake S, Fu Y, et al. Extravasated contrast material in penetrating abdominopelvic trauma: dual-contrast dual-energy CT for improved diagnosis–preliminary results in an animal model. Radiology. 2013; 268(3):738–42. [PubMed: 23687174]

51. Kumar V, Min JK, He X, Raman SV. Computation of Calcium Score With Dual-Energy Computed Tomography: A Phantom Study. J Comput Assist Tomogr. 2016 In Press.

52. Werncke T, Albrecht T, Wolf KJ, Meyer BC. Dual energy CT of the peripheral arteries: a phantom study to assess the effect of automatic plaque removal on stenosis grading. Rofo. 2010; 182(8): 682–9. [PubMed: 20198549]

53. Matsui K, Machida H, Mitsuhashi T, et al. Analysis of coronary arterial calcification components with coronary CT angiography using single-source dual-energy CT with fast tube voltage switching. Int J Cardiovasc Imaging. 2015; 31(3):639–47. [PubMed: 25407480]

54. Delesalle M-A, Pontana F, Duhamel A, et al. Spectral optimization of chest CT angiography with reduced iodine load: experience in 80 patients evaluated with dual-source, dual-energy CT. Radiology. 2013; 267(1):256–66. [PubMed: 23319663]

55. Stehli J, Fuchs TA, Singer A, et al. First experience with single-source, dual-energy CCTA for monochromatic stent imaging. European Heart Journal-Cardiovascular Imaging. 2015; 16(5):507–12. [PubMed: 25525062]

56. Lee N, Choi SH, Hyeon T. Nano-Sized CT Contrast Agents. Advanced Materials. 2013; 25(19): 2641–60. [PubMed: 23553799]

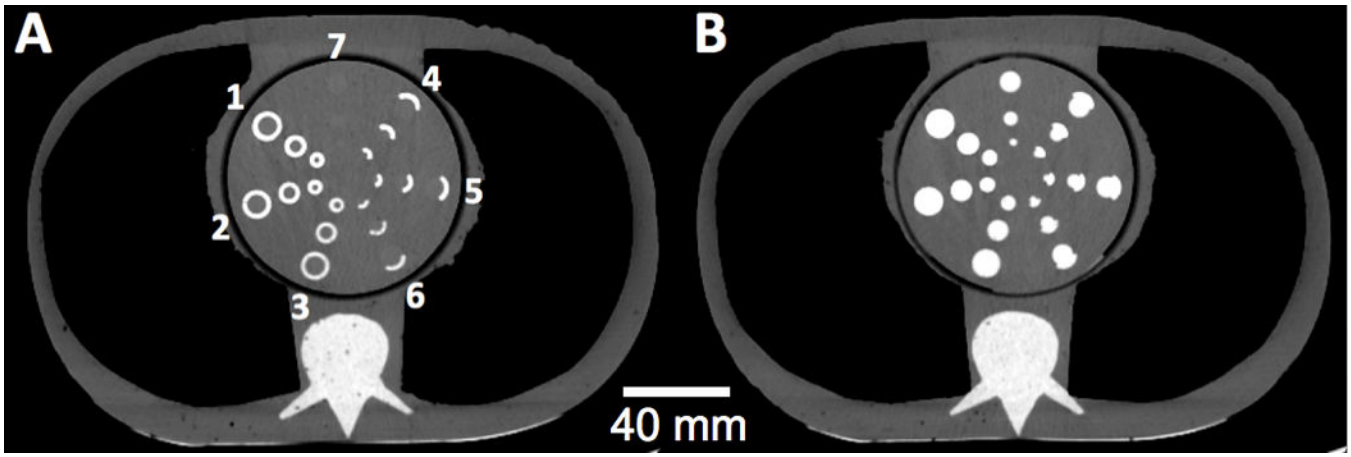

Figure 1.

Axial single energy CT images of the thorax phantom. Calcified walls of the simulated vessels were composed of 60, 40, and 20% hydroxyapatite by weight (radial arrangements of circumferential calcified walls labeled 1, 2, and 3, respectively, and arcs of calcified walls labeled 4, 5, and 6, respectively). Simulated vessel lumen diameters were 3, 6, and 9 mm for the innermost, mid, and outermost vessels, respectively. A) The simulated vessels were filled with water which, because of its similar x-ray attenuation as blood, enables straightforward scoring of the vessel wall calcifications. B) The simulated vessels were filled iodinated contrast material, severely limiting the ability to distinguish the calcifications from intravascular contrast. This demonstrates the requirement for the traditional two-phase coronary CT examination to obtain both calcium scores and a CT angiogram.

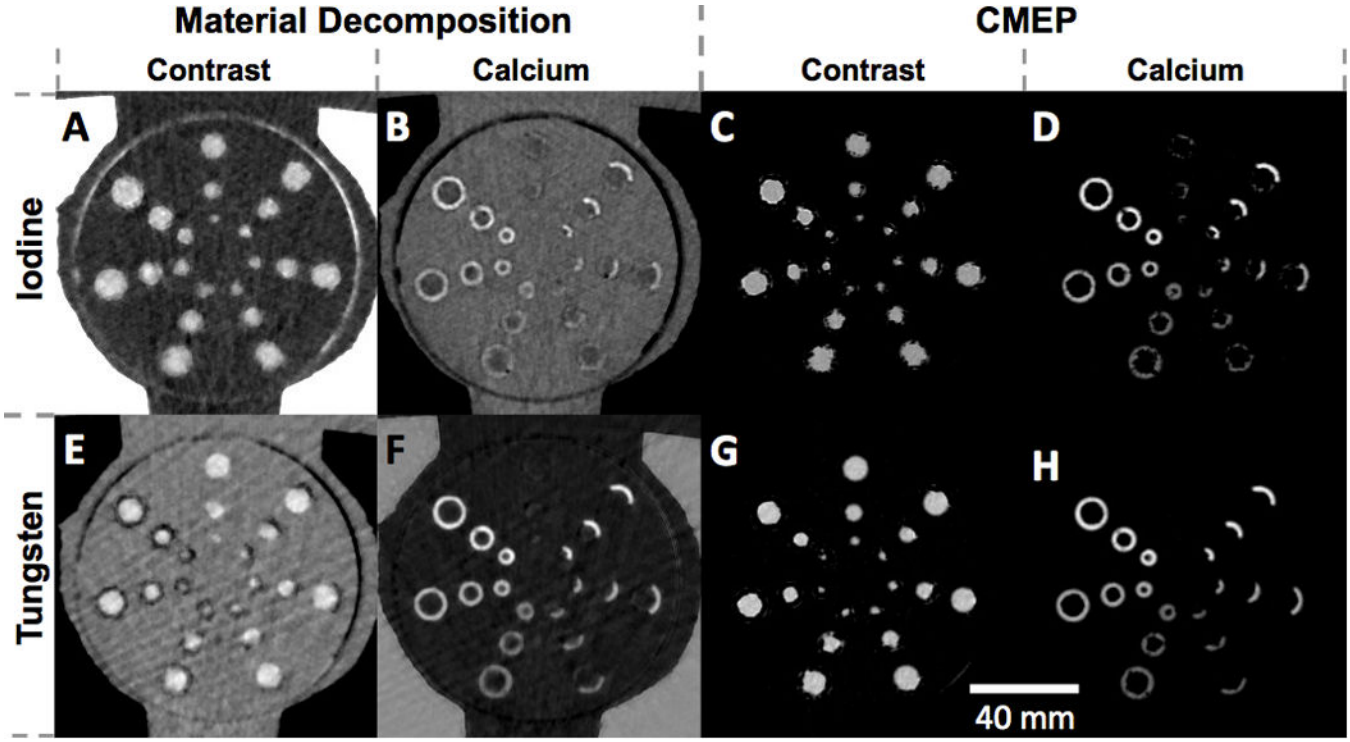

Figure 2.

Axial material-specific images. A) Iodine-calcium map generated by material decomposition (MD). B) Calcium-iodine MD. C) Iodine-calcium map generated by CMEP. D) Calcium-iodine CMEP. E) Tungsten-calcium MD. F) Calcium-tungsten MD. G) Tungsten-calcium CMEP. H) Calcium-tungsten CMEP. In all images the window width is scaled to the minimum and maximum pixel values observed within in the mediastinal insert for each dataset.

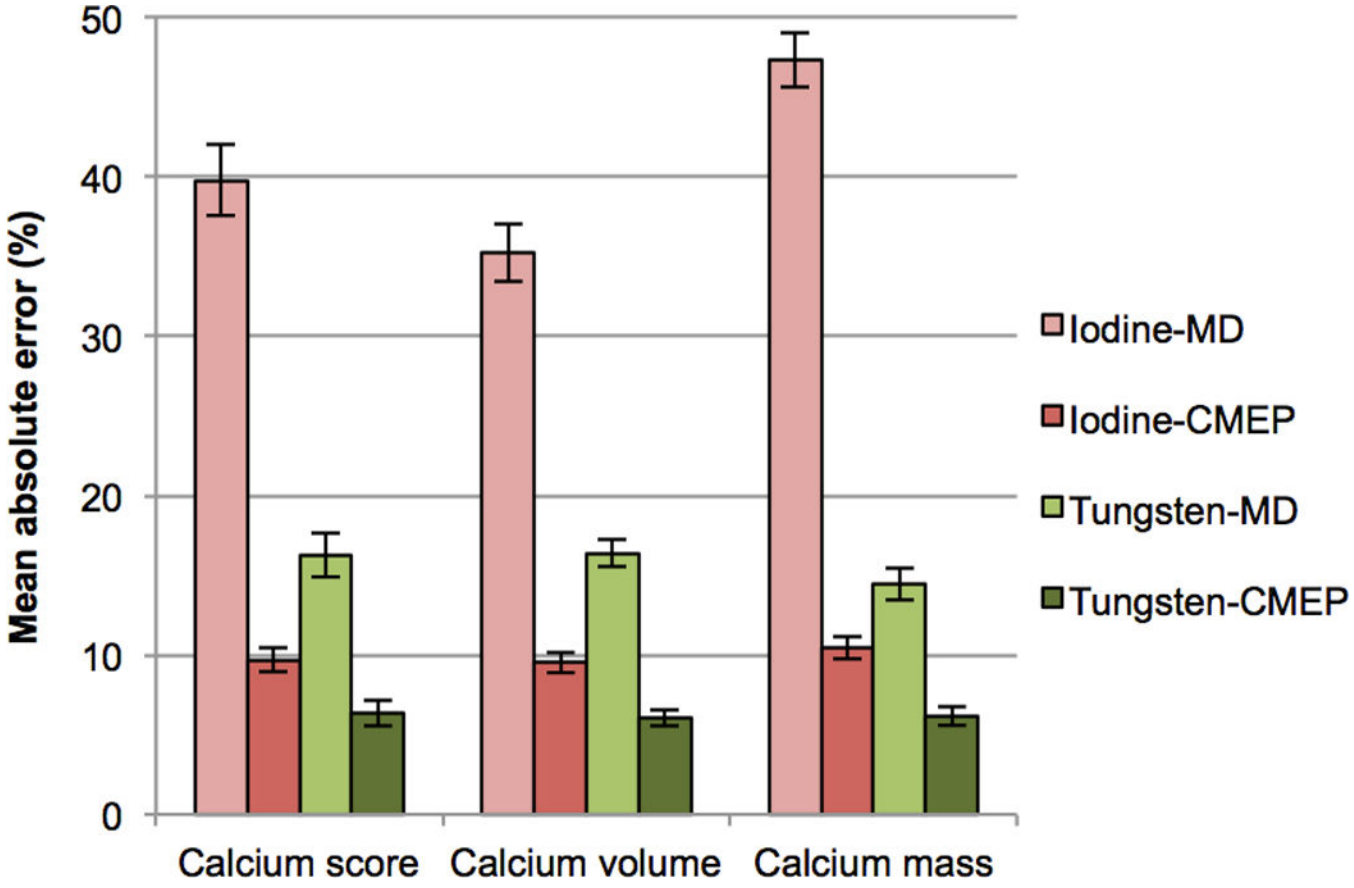

Figure 3.

Bar chart showing the mean absolute percentage errors for the four material separation datasets compared to the ground truth 120 kVp dataset. The same accuracy ranking is observed for the four datasets in each of the three calcium scoring methods. Error bars represent the standard error of the mean.

Table 1

Calcium scores among the five datasets for the 18 calcification types. Values for Water 120 kVp are the integer calcium scores, while the values for the other four datasets are relative errors compared to the Water 120 kVp dataset. Each value represents the mean among the eight images for each dataset. Values are shaded according to their percentage errors; the brighter the color the higher the error, with blue representing underestimation errors and red representing overestimation errors.

Type	HAP Density	Water 120 kVp (unitless)			Iodine-MD (%)			Iodine-CMEP (%)			Tungsten-MD (%)			Tungsten-CMEP (%)		
		3 mm	6 mm	9 mm	3 mm	6 mm	9 mm	3 mm	6 mm	9 mm	3 mm	6 mm	9 mm	3 mm	6 mm	9 mm
Concentric	20%	85	130	191	−60	−76	−76	−11	−20	−15	43	20	24	−2	−15	−11
	40%	127	210	314	−26	−20	−26	−14	−7	−12	21	12	10	5	−1	−3
	60%	136	235	342	−14	−17	−16	−8	−11	−11	14	12	9	6	1	−2
Eccentric	20%	31	47	66	−77	−77	−81	−11	−13	−3	24	37	−1	−17	−3	−20
	40%	52	83	111	−26	−34	−33	9	−9	−8	14	9	10	−8	−8	−5
	60%	54	97	127	−17	−25	−16	−4	−9	0	21	10	4	0	−3	−6

Table 2

Calcium volume scores among the five datasets for the 18 calcification types. Values for Water 120 kVp are the integer calcium volume scores, while the values for the other four datasets are relative errors compared to the Water 120 kVp dataset. Each value represents the mean among the eight images for each dataset. Values are shaded according to their percentage errors; the brighter the color the higher the error, with blue representing underestimation errors and red representing overestimation errors.

Type	HAP Density	Water 120 kVp (unitless)			Iodine-MD (%)			Iodine-CMEP (%)			Tungsten-MD (%)			Tungsten-CMEP (%)		
		3 mm	6 mm	9 mm	3 mm	6 mm	9 mm	3 mm	6 mm	9 mm	3 mm	6 mm	9 mm	3 mm	6 mm	9 mm
Concentric	20%	71	108	159	−48	−63	−64	−11	−20	−15	31	20	24	−2	−15	−11
	40%	79	131	196	−26	−20	−26	−14	−7	−12	21	12	10	5	−1	−3
	60%	85	147	214	−14	−17	−16	−8	−11	−11	14	12	9	6	1	−2
Eccentric	20%	26	41	55	−62	−67	−70	−7	−13	−3	24	38	13	−14	−3	−16
	40%	32	52	70	−18	−32	−33	9	−9	−8	14	9	10	−8	−8	−5
	60%	34	61	79	−17	−25	−16	−4	−9	0	21	10	4	0	−3	−6

Table 3

Calcium mass scores among the five datasets for the 18 calcification types. Values for Water 120 kVp are the integer calcium mass scores, while the values for the other four datasets are relative errors compared to Water 120 kVp. Each value represents the mean among the eight images for each dataset. Values are shaded according to their percentage errors; the brighter the color the higher the error, with blue representing underestimation errors and red representing overestimation errors.

Type	HAP Density	Water 120 kVp (unitless)			Iodine-MD (%)			Iodine-CMEP (%)			Tungsten-MD (%)			Tungsten-CMEP (%)		
		3 mm	6 mm	9 mm	3 mm	6 mm	9 mm	3 mm	6 mm	9 mm	3 mm	6 mm	9 mm	3 mm	6 mm	9 mm
Concentric	20%	169	249	365	−59	−72	−73	−12	−22	−18	38	18	19	−1	−15	−13
	40%	274	453	685	−44	−38	−44	−15	−8	−13	20	12	12	7	2	−1
	60%	383	661	980	−24	−27	−29	−5	−7	−9	13	10	7	6	3	0
Eccentric	20%	59	91	124	−71	−74	−77	−14	−16	−9	26	37	8	−14	−3	−18
	40%	104	175	234	−36	−47	−50	2	−11	−12	7	6	9	−8	−6	−4
	60%	137	267	372	−22	−37	−27	−2	−10	−4	12	7	1	1	−3	−6